Time Resolved Measurements Which Isolate the Mechanisms Responsible for Terahertz Glory Scattering from Dielectric Spheres

R. A. Cheville, R. W. McGowan, and D. Grischkowsky
School of Electrical and Computer Engineering and Center for Laser and Photonics Research, Oklahoma State University, Stillwater, Oklahoma 74078
(Received 24 June 1997)

The surface-wave scattering processes responsible, in part, for the optical glory have never been compared with theoretical predictions. Here, THz impulse ranging is used to measure the time domain impulse response of spherical targets with sufficiently high temporal resolution to permit the surface-wave contribution to the total impulse response to be isolated. The first direct experimental comparison for the surface wave with Mie theory as well as the surface-wave approximation of van de Hulst is performed. Interference of the surface waves from a dielectric sphere is shown to lead to the frequency and angular intensity dependence of the THz glory. [S0031-9007(97)04970-3]

PACS numbers: 42.25.Fx

There has been a great deal of interest in determining wave scattering from spherical particles since the initial work of Clebsch in 1861, the best known of which is that of Mie in 1908 [1]. Mie's theory allows the exact determination of the frequency dependent scattered electric field expressed as an infinite summation. Much of this interest has been due to the spectacular optical effects of the rainbow and the lesser known glory observed due to scattering from water droplets in the atmosphere. The glory is an enhancement of scattered radiation in the backwards direction and appears as concentric rings of colored light when suspended water droplets are illuminated from directly behind the observer. It is most commonly seen around the shadow of an airplane flying over clouds.

The determination of scattering from dielectric spheres is accomplished by a variety of methods that can be broadly separated into computational/theoretical and experimental techniques. The volume of theoretical work on electromagnetic scattering is vast for both frequency domain [2,3] as well as time domain [4,5] calculations. On the experimental side, comparatively less work has been done for radar [6,7] and optical [8–10] frequencies. If both the amplitude and phase of the scattered electric field can be determined, time and frequency measurements provide the same information due to the linear nature of electromagnetic scattering. In the frequency domain, where the Mie theory provides an exact solution, it is difficult to determine the physical mechanisms responsible for the observed features. Measurements in the time domain, however, can provide more physical insight, since scattering centers and mechanisms may be identified by the time of arrival of the scattered pulses [11]. For this reason, several recent efforts have focused on constructing and characterizing impulse ranges using both electronic [12] and optoelectronic [13,14] generation techniques. The ability to isolate the scattered wave forms in time allows spectral analysis of individual scattering mechanisms which can then be compared with theory. With sufficient temporal resolution, the frequency response due to various scattering mechanisms can be disentangled from the much more complex overall scattering signature.

We have developed a laboratory-scale ranging test bed for generating and detecting optoelectronically generated THz pulses [7,14]. This ultrawide band system, producing pulses with frequency components extending from 100 GHz to beyond 2 THz, is ideally suited for studying time dependent scattering from dielectric spheres. The use of suitable beam shaping THz optics permits plane wave excitation. The time dependent scattered electric field is measured with 0.3 ps resolution and high signal-to-noise ratio, and permits unambiguous identification of specular, surface-wave, and axial scattering features of the impulse response from the sphere. The ability to temporally isolate the surface wave permits the first experimental verification of several surface-wave scattering theories.

The experimental setup used for these high resolution studies is similar to that published previously [7,14], and is shown in Fig. 1. A sub-100 fs optical pulse generated by a passively mode-locked Ti:Al_2O_3 laser is focused on a dc biased, coplanar transmission line structure; the subsequent acceleration of optically generated carriers produces the THz pulse. A 30 μm dipole antenna fabricated on radiation damaged silicon on sapphire with a subpicosecond carrier lifetime is used as the detector. An optical pulse incident on the dipole gap gates the detector, producing a current proportional to the bias from the incident THz pulse. Delay of the optical gate pulse permits the time dependent THz electric field to be determined. System characterization is accomplished by replacing the target with a 2.5 cm diameter brass sphere as a reference reflector having a unity, frequency independent response. The ratio of the measured electric field scattered from a spherical target to that of the spherical reference reflector directly determines the complex scattering function of the target, $E_{\mathrm{meas}}(\omega)/E_{\mathrm{ref}}(\omega) = T(\phi, \omega, r)$.

0031-9007/98/80(2)/269(4)$15.00 © 1998 The American Physical Society

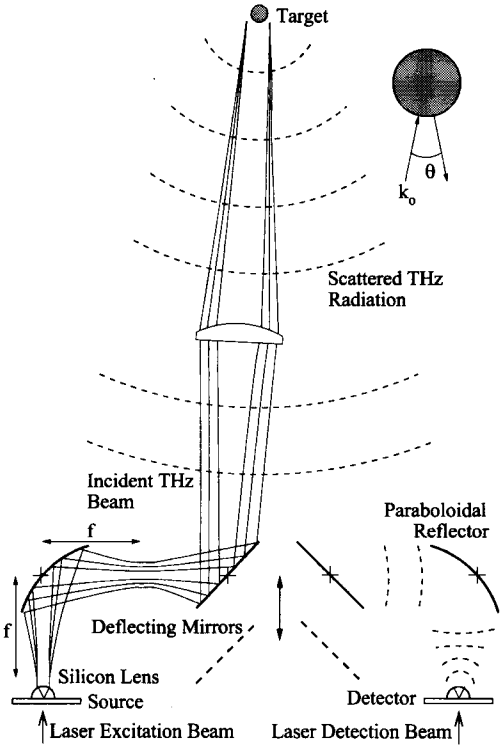

FIG. 1. THz impulse ranging experimental setup. The electric fields are polarized in the plane of the diagram.

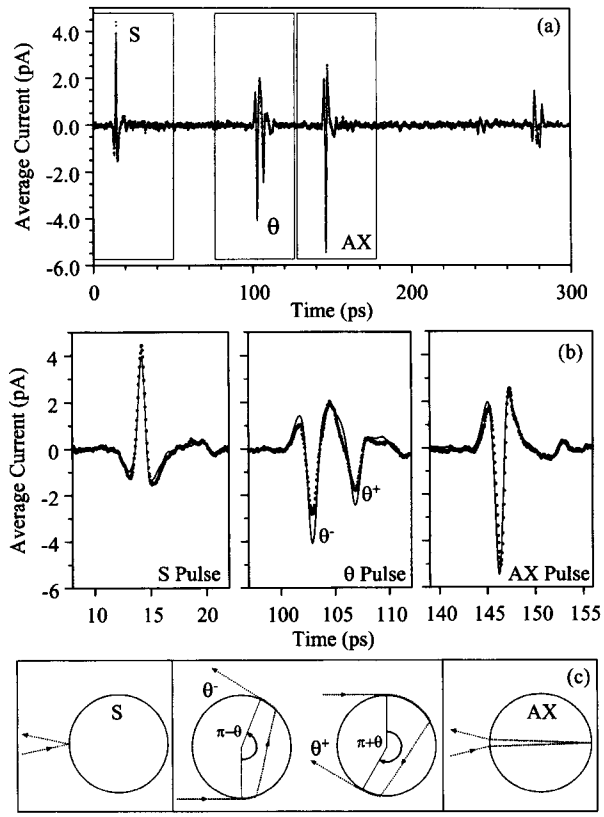

FIG. 2. (a) Measured scattered THz pulse from a 6.35 cm diameter alumina sphere (solid dots) and calculated pulse structure (solid line). (b) Detail of measurement and fit for specular, surface wave, and back axial reflections. (c) Geometrical optics representations of the specular (S), surface (θ), and back axial (AX) reflections.

Measurements were performed on an alumina sphere with a diameter of 6.35 mm. The time dependent scattered electric field from the sphere was measured in the far field. The scattered pulse is shown in Fig. 2(a) as individual points. This measurement consisted of eight individual 6000 point scans with a 50 fs temporal resolution averaged to improve the signal-to-noise ratio. Figure 2(b) shows a detail of the features appearing at 15, 105, and 145 ps.

We compare the measured scattered electric field pulse with that calculated from a Mie theory numerical analysis in the far field approximation [15] in Fig. 2. The Fourier amplitude at frequency ω of the scattered field measured at the detector is given by

$$E_{\mathrm{scat}}(\theta,\omega) = E_{\mathrm{inc}}(\omega)\,\frac{e^{ik_0 r}}{k_0 r}\,T_{\mathrm{calc}}(\omega,\theta), \qquad (1)$$

where $k_0 = 2\pi/\lambda$ is the wave vector in free space. The scattered pulse in the time domain is obtained by the inverse fast-Fourier transform of $T_{\mathrm{calc}}(\theta,\omega,r)$ multiplied by the complex amplitude spectrum of the reference pulse $E_{\mathrm{ref}}(\omega)$. The calculated response from the dielectric sphere is plotted as a solid line with the data points for the time dependent scattered pulses in Figs. 2(a) and 2(b).

Since the scattering signatures consist of well resolved and temporally separated pulses, each of these returns can be identified with a physical scattering mechanism [7]. The first pulse, labeled "S" in Figs. 2(a) and 2(b), is due to specular reflection from the front surface of the sphere. The next feature "θ" consists of two closely spaced pulses and is due to a surface wave of the type first proposed by van de Hulst [3] which is excited by the portion of the THz beam which strikes the sphere at grazing incidence as shown in Fig. 2(c). The time delay between the two pulses "θ^+" and "θ^-" is due to the bistatic angle of $\theta = 11°$ resulting in a path length difference for the two surface waves, which travel clockwise and counterclockwise around the sphere making rotations of $\pi + \theta$ and $\pi - \theta$ radians, respectively. The pulse labeled "AX" is due to a back axial reflection, which is the portion of the incident pulse transmitted into the target and then reflected from the back side of the sphere.

Because the scattered pulses are well separated in time, it is possible to perform Fourier analysis on the pulse from each scattering mechanism. Figure 3(a) shows the measured amplitude spectrum of the scattered pulse train of Fig. 2(a). The complexity of this spectrum illustrates the difficulty in obtaining information about a single scattering mechanism from frequency domain measurements; the measured signal contains components from, and interactions between, all of the scattering mechanisms. In contrast to the complex spectrum of Fig. 3(a), the slowly varying amplitude spectra of the temporally isolated S, θ,

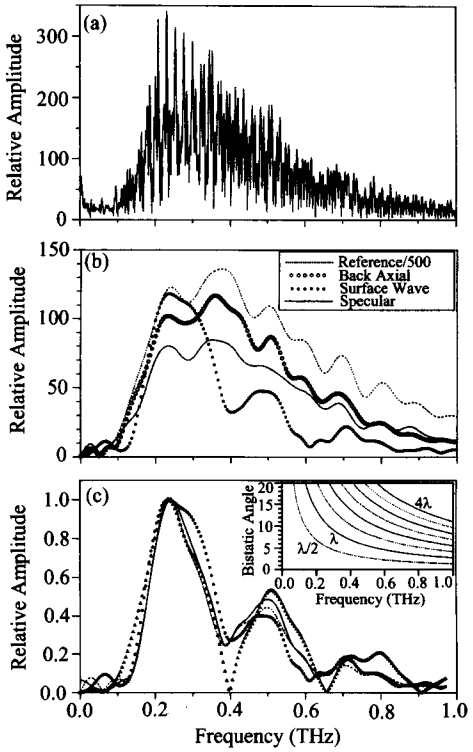

FIG. 3. (a) The amplitude spectrum of the measured scattering shown in Fig. 2(a). (b) Numerical Fourier transforms of the specular reflection S (solid line), surface wave θ (solid dots), and axial (open circles) scattered pulses from Fig. 2(b). Also shown is the amplitude spectrum of the reference pulse (dashed line) scaled down by a factor of 500. (c) Fit of the van de Hulst model (open triangles), the geometrical optics model (dashed line), and the Mie theory fit (solid line) compared to the measured surface-wave spectrum (solid dots). The inset shows the constructive and destructive interference contours which lead to the THz glory.

and AX reflections from the alumina sphere of Fig. 2(b) *are shown in Fig. 3(b), together with the amplitude spectrum* of the measured reference pulse reduced in scale by 500 times. The amplitude spectra of the specular and back axial reflections are similar to the reference spectra, although with increasing frequency the S spectrum crosses over the AX spectrum due to the absorption of alumina. In contrast, the contribution from the surface wave shows a frequency dependent oscillatory structure.

An explanation of this oscillatory structure and the effect of the surface wave was first proposed by van de Hulst [3] through numerical approximations to the Mie series in order to explain the optical glory seen in back illumination from water droplet clouds. In this case, the scattering coefficient $S(\omega, \theta)$ due to the surface wave is obtained from the Mie theory by applying the localization principle [3]; considering only those terms corresponding to a ray striking at grazing incidence:

$$S(\omega, \theta) = \tfrac{1}{2}C_2[J_0(u) + J_2(u)] + \tfrac{1}{2}C_1[J_0(u) - J_2(u)], \tag{2}$$

where $u = 2\pi a\theta/\lambda$, and C_1 and C_2 are constants [3]. For water droplets with $n \cong 1.33$, van de Hulst estimated the ratio of C_1/C_2 to be in the range $-\frac{1}{4}$ to $-\frac{1}{5}$. The scattered electric field amplitude for the surface-wave contribution is given by the spectrum of the reference pulse multiplied by the scattering coefficient and an empirical amplitude constant A, i.e., $|E_{\text{surf}}(\omega)| = |A \times E_{\text{ref}}(\omega) \times S(\omega, \theta)|$.

The calculated spectra from the surface wave determined from Eq. (2) is plotted as open triangles on top of the data (solid dots) in Fig. 3(c), with the best fit for $C_1/C_2 \cong -0.5$. Acceptable fits are obtained for C_1/C_2 in the range from -0.35 to -0.75. Despite the approximations made in this analysis, agreement is surprisingly good across the entire bandwidth. We believe this is the first experimental verification of the frequency dependent scattering due expressly to the surface-wave contribution.

To understand the physical mechanisms of scattering, several authors have compared Mie theory with a simplified geometrical optics model [4,16]. The delay between the specular reflection pulse and surface-wave scattered pulse in this geometrical optics model for θ, in radians, is given by

$$\Delta\tau = \frac{1}{c}\{2a + an_{\text{eff}}[(\pi \pm \theta) - 2\gamma] + 2Nna \sin\gamma\}, \tag{3}$$

where γ is determined by the critical angle, $\alpha_c = \arcsin(1/n)$, with $\gamma = \pi/2 - \alpha_c$. The index of refraction n_{eff} determines the surface-wave velocity, c is the velocity of light in free space. A previous publication [7] fit the pulse return times as a function of diameter of fused silica cylinders and determined n_{eff} to lie in the range 0.95 to 1.12, indicating that, for cylinders, the surface wave was weakly coupled and propagated with a velocity near that of free space. This analysis did not address pulse reshaping and attenuation.

In the current study, the surface wave appears severely reshaped compared to the specular and reference pulses. For our bistatic angle, $\theta = 11°$, this reshaping is due to the fact that the surface wave consists of two pulses, θ^+ and θ^- shown in Fig. 2. From Eq. (3), the optical path length on the sphere D traveled by these two surface waves is $D_{\pm\theta} = (\pi \pm \theta - 2\gamma)an_{\text{eff}}$. For the alumina sphere, the distances the θ^+ and θ^- waves travel on the surface are 2.66 and 1.44 mm, respectively. These distances, together with the measured time delay of 4.0 ps between θ^+ and θ^-, gives $n_{\text{eff}} = 0.985 \pm 0.02$. It is clear from the difference in amplitudes of the two pulses that there is significant loss and dispersion associated with the surface wave.

The geometrical optics model of Eq. (3) may be used to describe the spectrum of the surface wave. Because of the different optical path lengths, the $+\theta$ and $-\theta$ pulses emerge separated in time with phase shifts of $\exp(ik_0D_{\pm\theta})$. The frequency dependent scattered electric

field is given by the superposition of these two pulses:

$$E_{\text{meas}}(\theta,\omega) = AE_{\text{ref}}(\omega)[e^{i\frac{2\pi a}{\lambda}n_{\text{eff}}(\pi-2\gamma N)}e^{i\frac{4\pi a}{\lambda}n\sin\gamma} \times (e^{i\frac{2\pi a}{\lambda}\theta n_{\text{eff}}} + e^{-i\frac{2\pi a}{\lambda}\theta n_{\text{eff}}})], \quad (4)$$

where n_{eff} is a frequency dependent complex index describing changes in both phase and amplitude. The empirical constant A is used to normalize the measured scattering to the amplitude of the incident pulse and is a measure of the coupling efficiency of the incident electric field to the surface wave. Numerically fitting the measured amplitude spectrum from the surface wave to the geometrical model of Eq. (4) gives the fit shown as the dashed line in Fig. 3(c) with $n_{\text{eff}} = 0.98 + 0.08i$. The accuracy of the values obtained by this numerical fit are expected to be on the order of $\pm 5\%$ for the real part and $\pm 15\%$ for the imaginary part of n_{eff}.

This fit compares quite favorably with that obtained from a numerical Mie theory analysis shown as the solid line in Fig. 3(c) obtained from the time domain fit to the θ pulse data of Fig. 2(b). The slight offset of the positions of the predicted and measured valleys at approximately 0.4 and 0.6 THz can be removed by using a frequency dependent real part for n_{eff}. The imaginary part of n_{eff} is expected to have a $\lambda^{2/3}$ dependence [17]; better data will be needed to verify this dependence.

Note that the geometrical optics model [Eq. (4)] can be written in the same form within a constant as the van de Hulst approximation of the Mie scattering surface-wave terms [Eq. (2)] for $C_1/C_2 = -3$ and $n_{\text{eff}} = 1 + 0i$. The geometrical optics model presented here is intuitive, fits the data well, and has been used by many previous authors [4,16]. However, several caveats should be made for the lower frequencies comprising the THz pulse since geometrical optics assume that the scatterer is considerably larger than the wavelength, and in this investigation the size parameter $k_0 a$ ranges from 6 to 130 across the bandwidth of the THz pulse. Also, though surface-wave propagation is modeled by a term of the form e^{ikx}, it will be dependent upon the curvature of the surface which would be incorporated in this model by a size dependent n_{eff}.

The scattered electric field of Eq. (4) also shows a strong dependence on θ. For backscattering ($\theta = 0$) the optical path for all frequencies is equal, and constructive interference occurs at all frequencies. As θ changes, the relative optical path difference ΔD between the θ^+ and θ^- pulses varies as $\Delta D = 2\theta a n_{\text{eff}}$. In this case, constructive interference occurs for $\Delta D = 2m\lambda$ or $\theta = m\lambda/an_{\text{eff}}$ and destructive interference for $\Delta D = (2m+1)\lambda/2$ with $m = 0, 1, \ldots$. This interference is independent of the index of the sphere, which is also the case for the frequency dependent oscillations of Eq. (2). This angle dependent oscillatory structure is similar to the optical glory. As shown by the inset of Fig. 3(c), the contours on which constructive (solid lines) and destructive (dashed lines) interference of the θ^+ and θ^- waves occurs leads to a "rainbow" variation of the THz radiation as a function of angle. For an unpolarized incident field, this leads to a ringlike structure of the various frequency components of THz radiation in the backscattering direction. Note that the frequency and angle dependence of the THz glory observed here is almost entirely due to the surface waves, unlike the optical glory for which many competing physical effects contribute [17].

This work was supported in part by the National Science Foundation under Grants No. PHY-9422952 and No. ECS-9521030 and the Army Research Office under Grant No. DAAH04-96-1-0396.

[1] N. A. Logan, Proc. IEEE **53**, 773 (1965).
[2] H. M. Nussenveig, J. Math. Phys. (N.Y.) **10**, 82 (1969); **10**, 125 (1969).
[3] H. C. van de Hulst, *Light Scattering by Small Particles* (Wiley, New York, 1957).
[4] A. Itoh and T. Hosono, Electron. Commun. Jpn. 2 **78**, 10 (1995).
[5] E. E. M. Khaled, D. Q. Chowdhury, S. C. Hill, and P. W. Barber, J. Opt. Soc. Am. A **11**, 2065 (1994).
[6] D. Kralj and L. Carin, Appl. Phys. Lett. **62**, 1301 (1993).
[7] R. A. Cheville, R. W. McGowan, and D. Grischkowsky, IEEE Trans. Antennas Propag. **45**, 1518 (1997).
[8] D. S. Langley and M. J. Morrell, Appl. Opt. **30**, 3459 (1991).
[9] T. S. Fahrlen and H. C. Bryant, J. Opt. Soc. Am. **58**, 304 (1968).
[10] D. S. Langley and P. L. Marston, Phys. Rev. Lett. **47**, 913 (1981).
[11] A. K. Dominek, L. Peters, Jr., and W. D. Burnside, IEEE Trans. Antennas Propag. **35**, 305 (1987).
[12] M. Morgan, IEEE Trans. Antennas Propag. **42**, 840–846 (1994).
[13] L. Carin, in *Ultra-Wideband, Short-Pulse Electromagnetics,* edited by H. Bertoni (Plenum, New York, 1993), pp. 37–49.
[14] R. A. Cheville and D. Grischkowsky, Appl. Phys. Lett. **67**, 1960 (1995).
[15] D. E. Barrick, in *Radar Cross Section Handbook,* edited by G. T. Ruck (Plenum Press, New York, 1970), Vol. 1.
[16] J. Rheinstein, IEEE Trans. Antennas Propag. **16**, 89–97 (1968); H. Inada, Appl. Opt. **13**, 1928 (1974).
[17] V. Khare and H. M. Nussenveig, Phys. Rev. Lett. **38**, 1279 (1977).